nature photonics

ARTICLES

PUBLISHED ONLINE: 19 DECEMBER 2010 | DOI: 10.1038/NPHOTON.2010.284

Coherent coupling between distant excitons revealed by two-dimensional nonlinear hyperspectral imaging

J. Kasprzak[1]*†, B. Patton[1]†, V. Savona[2] and W. Langbein[1]*

Coherent coupling between distant two-level systems is a fundamental process in several physical contexts, from natural photosynthesis to quantum-information processing, where it enables two-qubit operations. For quantum information, qubits based on electronic degrees of freedom in a solid-state matrix are sensible candidates for scalable, integrated implementations. Clarifying the mechanisms underlying coherent coupling in solids is therefore an essential step in the development of such technology. Here, we demonstrate the existence of a long-range coherent coupling mechanism between individual localized excitons in a 5 nm GaAs/AlGaAs quantum well, introducing the novel tool of two-dimensional nonlinear coherent hyperspectral imaging. The coupling is shown to arise due to a biexcitonic renormalization, rather than a transition dipole (Förster) interaction. The long-range nature of the coupling is attributed to the existence of spatially extended exciton states up to the micrometre range, which are admixed in the biexciton state, as revealed in nonlinear imaging.

Although a variety of approaches are used to generate qubits (quantum two-level systems), those that are to be integrated into practical quantum-information processing devices[1] will most likely be embedded into a solid state matrix[2–5]. Electron pairs[6–8] and individual excitons[9,10] confined in semiconductor quantum dots are both systems to have been investigated in this context. The next essential step towards the semiconductor implementation of quantum information technology is to take advantage of coherent coupling mechanisms between distant qubits to enable controlled two-qubit operations[11]. For this, it is important to understand the physical mechanisms underlying long-range electronic coupling in semiconductors. Here, we study the model system of individual localized excitons in a narrow GaAs/AlGaAs quantum well.

Substantial coupling of excitons to the light field to enable their optical coherent manipulation and measurement comes at the expense of subnanosecond coherence times. Coherent manipulation on this fast timescale is possible with the tools of coherent ultrafast spectroscopy. Specifically, the recently developed technique of heterodyne spectral interferometry[12,13] (HSI) is capable of detecting a resonantly excited transient coherent nonlinear response, such as four-wave mixing (FWM), in individual quantum systems (see Methods and Supplementary Appendix C). This combines a heterodyne detection scheme[14,15], which allows the rejection of the incoherent background and efficient discrimination of the selected nonlinear signal, with spectral interferometry[16], permitting retrieval of the spectral response in both amplitude and phase. Obtaining the response in both amplitude and phase allows its analysis in both frequency and time domains[17,18]. Additionally, because HSI is a multipulse technique, analysis of the dependence on the time delay between excitation pulses allows the application of two-dimensional spectroscopy in the optical frequency range on single excitons[12,13] (a technique previously restricted to large ensembles[19–21]) to observe and quantify coherent coupling within a small ensemble of excitons.

Earlier multidimensional spectroscopy techniques were limited to a spatial resolution of ~100 μm, and were not sensitive enough to measure individual quantum systems. For example, two-dimensional nuclear magnetic resonance (NMR), which can measure coherent coupling of nuclei[22], requires more than 10^{20} nuclei. Even two-dimensional optical spectroscopy, used to measure electronic coupling, uses 10^{16} molecules[19]. The combination of submicrometre-scale imaging with multidimensional spectroscopy sensitive to individual quantum systems represents a step change, providing a powerful tool for resolving many open questions in solid-state physics. Here, we demonstrate its capabilities by assessing the coherent coupling between excitonic states with two-dimensional FWM and ascertain the underlying physical mechanism.

Representative FWM hyperspectral images of localized excitons are given in Fig. 1 (see also Supplementary movies A and B) for different sample regions with low (Fig. 1a–c) and high (Fig. 1d–f) densities of localized exciton states. Individual excitons can be identified by the spatially and spectrally localized nature of their FWM responses. To facilitate the discrimination of individual states, centre energies were encoded as false colours. The difference in the density of localized excitons in the two regions is evident: within the displayed energy range of 200 μeV, approximately one exciton of significant oscillator strength is detected in the low-density region, and about ten excitons in the high-density region. Although in the low-density region the excitons are localized to within the spatial resolution, in the high-density region, spatially extended structures[23] (up to a few micrometres in length) with a resonance energy that is constant (within an error of a few μeV) can be observed (Supplementary Fig. B).

The presence of spatially and spectrally close-lying exciton states suggests the possibility of coherent coupling between them. To investigate the strength and mechanism of such coupling, we used two-dimensional spectroscopy to measure the FWM response as a function of delay time. Figure 2a shows the FWM amplitude

[1]School of Physics and Astronomy, Cardiff University, The Parade, Cardiff, CF24 3AA, UK, [2]Institute of Theoretical Physics, Ecole Polytechnique Fédérale de Lausanne EPFL, CH-1015 Lausanne, Switzerland; †Present address: Néel Institute, CNRS/UJF, 25 rue des Martyrs, 38042 Grenoble, France (J.K.), Centre for Quantum Photonics, H. H. Wills Physics Laboratory, University of Bristol, Tyndall Avenue, Bristol BS8 1TL, UK (B.P). *e-mail: jacek.kasprzak@grenoble.cnrs.fr; langbeinww@cf.ac.uk

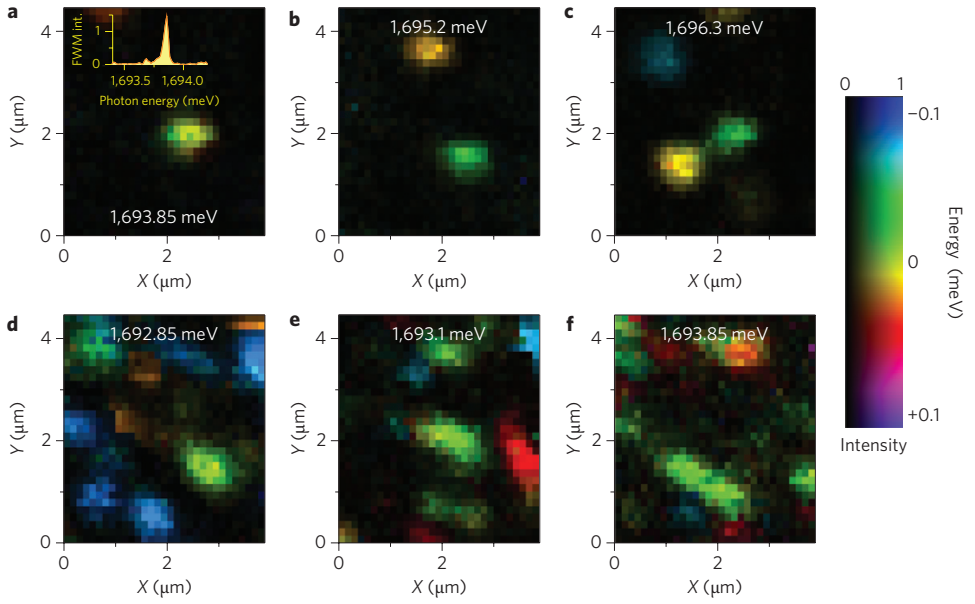

Figure 1 | Hyperspectral spatial imaging of FWM from individual excitons localized in monolayer islands of a 5 nm GaAs/AlGaAs quantum well. a–f, Two different regions with low (**a–c**) or high (**d–f**) island density are investigated (see also Supplementary Movies A, B and Supplementary Figs A–C). Direction *X* is along [1$\bar{1}$0], *Y* is along [110] and $\tau = 0$. Linear polarization configuration ($\rightarrow$, $\rightarrow$, $\rightarrow$) along [1$\bar{1}$0]. The FWM spectrum $|R_s^{-1,2}(\omega_3, 0)|^2$ in a spectral region around a chosen centre energy was fitted by a Lorentzian. The resulting peak area is displayed as brightness and the peak energy relative to the indicated centre energy is indicated by the hue of the colour over a range of $\pm$100 μeV (see colour bar). Inset to **a**: example of the FWM intensity spectrum at the spatial centre of the observed spot. A constant hue indicates a single exciton state. In the low-density region with an area of 16 μm^2, we detect 52 strong transitions over the range 1.69–1.7 eV, which represent the ground states (with a high oscillator strength) of excitons localized in troughs with thicknesses of 17 monolayers surrounded by 16-monolayer barriers[27]. This corresponds to an average of one state per energy interval of 0.2 meV, and an average inter-exciton distance of 0.6 μm.

$|R_s^{-1,2}(\omega_3, \tau)|$ as a function of the detected photon energy $\hbar\omega_3$ and delay τ, measured in the low-density region for linear polarization[24] ($\rightarrow$, $\rightarrow$, $\rightarrow$) along [1$\bar{1}$0]. The spectrum is dominated by the excitonic transition X_1 at $\omega_3 = 1.6943$ eV. In the vicinity of X_1, weaker transitions X_2, X_3 and X_4 are visible as beats versus delay, as highlighted in the inset to Fig. 2a. These oscillations are not a manifestation of coherent coupling, as shown below, but are due to polarization interference[25] occurring between the spectral wings of X_1, and the weaker resonances X_2, X_3 and X_4. With varying τ the latter acquire phase shifts with respect to X_1, resulting in oscillations with a period inversely proportional to their spectral separation from X_1. For example, at X_2, with a detuning of $\delta = 0.45$ meV to X_1, a corresponding beat period of 9 ps $\approx h/\delta$ is measured. Weaker FWM resonances, of similar strength both for positive and negative τ, are observed on the lower energy side. These are bound biexciton transitions XX_1 and XX_4 coupled to X_1 and X_4.

The HSI technique recovers the FWM both in amplitude and phase, so the delay τ can be Fourier-transformed to the conjugated frequency ω_1 (for $\tau > 0$): $R_s^{-1,2}(\omega_3, \omega_1) = \int R_s^{-1,2}(\omega_3, \tau)e^{-i\omega_1\tau}d\tau$, as discussed in ref. 12 (also see Supplementary Fig. D and Appendix B). In the resulting $R_s^{-1,2}(\omega_3, \omega_1)$ the first- and third-order resonances of the system are separated, which is key to quantifying the strength and type of coupling (similar to the multidimensional spectroscopy developed for NMR studies[22]). The $R_s^{-1,2}(\omega_3, \omega_1)$ representation (two-dimensional FWM) of the data in Fig. 2a is shown in Fig. 2b. The dominant feature is a diagonal line of peaks (labelled 'X states'); these signals have equal first- and third-order frequencies. First-order polarization resonances are single excitons, and diagonal signals are therefore due to a third-order polarization on the same single exciton as the first-order polarization. Such diagonal signals dominate in the low-density region (Fig. 1a–c), where the average distance between localized excitons is large and extended excitons are not observed, so that coherent coupling between excitons is expected to be suppressed. Each exciton resonance is accompanied by a weak resonance at the same ω_1, but at ω_3 some 5 meV below. These resonances at different ω_3 are transitions from excitons to bound biexcitons, which form a second approximate diagonal that is redshifted by the biexciton binding energy of (5.0 ± 0.1) meV (ref. 26). Corroboration of the biexcitonic origin of these peaks is provided by the observation of a π-shift between the phase of 0–X and X–XX transitions (as discussed later), shown by the green trace in Fig. 2b. From the measured lineshapes, homogeneous linewidths of ~10 μeV for the 0–X transitions and ~10–20 μeV for the X–XX transitions are inferred, taking into account the spectrometer resolution. Using the amplitude of the FWM and the estimated homogeneous linewidths, we could determine the oscillator strength of the X–XX transitions relative to the 0–X transition, and found it to be 1.7 to 17 times weaker. We also observed instances of single excitons with transitions to multiple bound biexcitons, like the doublet XX_1. The above features are indicative of a system with a Coulomb correlation energy comparable to the exciton confinement energy of ~10 meV given by a monolayer thickness variation[27], so biexcitons in these structures are in a regime between weak and strong confinement. In the strong confinement limit, biexcitons are described by a product wavefunction of two excitons, yielding the equal oscillator strength of the 0–X and X–XX transitions. Instead, if biexciton states contain significant admixtures of wavefunctions of other single exciton states, the X–XX transition is weaker. Spatial imaging of the XX_1 and XX_4 energies showed that the transitions are co-localized to their respective excitons, as expected.

As single excitons are localized in a disorder-induced island or terrace, which, in general, has non-cylindrical spatial symmetry, a fine-structure splitting[28] is expected. Indeed, by investigating with a ($\nearrow$, $\nearrow$, $\nearrow$) configuration, we find that the X_1 transition in Fig. 2b is split into [110] and [1$\bar{1}$0] polarizations, with the former having 54 μeV lower energy than the latter, inducing polarization dynamics[24,29]. Two-dimensional FWM $|R_s^{-1,2}(\omega_3, \omega_1)|$ in the

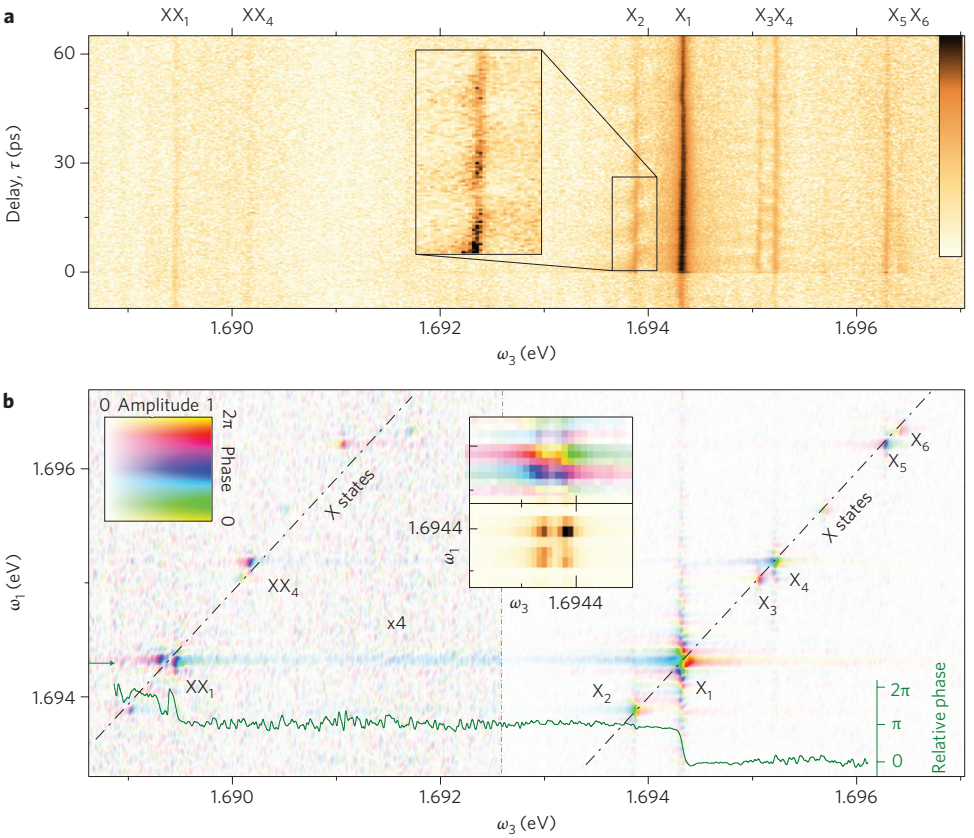

Figure 2 | Coherent coupling features observed in two-dimensional FWM at the region with low exciton density. a, Spectrally resolved FWM amplitude $|R_s^{-1,2}(\omega_3, \tau)|$ as a function of delay τ measured for the low-density region shown in Fig. 1a–c. Logarithmic colour scale shown over a factor of 200. Linear polarization configuration (→, →, →). Inset: zoom of the polarization interference between X_1 and X_2. **b**, Amplitude (saturation) and phase (hue) of the two-dimensional FWM $R_s^{-1,2}(\omega_3, \omega_1)$ resulting from **a** after Fourier transformation along τ. Amplitude is on a linear scale, magnified by a factor of four for $\omega_3 < 1.6926$ eV. Single excitons (X_1–X_6) and associated biexciton transitions are observed. The green trace shows the phase at $\omega_1 = 1{,}694.33$ meV. A π shift between the signal of X_1 and XX_1 is seen. (For an intensity-only representation of **b** see Supplementary Fig. E.) Inset: two-dimensional FWM of the X_1 transition for (↗, ↗, ↗) polarization configuration, which exhibits a fine-structure splitting. Lower inset: amplitude on a linear scale from zero (colour map as in **a**). Upper inset: amplitude and phase-resolved colour map as in **b**.

vicinity of the fine-structure split exciton retrieved under these conditions is shown in the inset of Fig. 2b. Strong coherent coupling (coupling exceeding the decoherence) is demonstrated by the off-diagonal signal of equal amplitude to the diagonal. Each polarization component not only creates a third-order signal on itself (diagonal peaks), but also creates a third-order response of the partner in orthogonal polarization, resulting in a pair of peaks with $\omega_1 \neq \omega_3$, (that is, off-diagonal).

To enhance coherent coupling between excitons in different spatial states, we decreased the average spatial exciton separation by moving to the region of higher exciton density shown in Fig. 1d–f, for which the measured $|R_s^{-1,2}(\omega_3, \tau)|$ is presented in Fig. 3a. The pronounced beating versus τ indicates the presence of coherent coupling, which is confirmed in the corresponding $R_s^{-1,2}(\omega_3, \omega_1)$ representation shown in Fig. 3b. Similar to the low-density region shown in Fig. 2b, there is a diagonal line of peaks from all the excitons probed by the excitation. Additionally, off-diagonal peaks between some of the excitons (insets 1, 2 and 3, Fig. 3b) are present, showing third-order polarization resonances driven by different first-order polarization resonances (Supplementary Fig. G). Pairs of coupled exciton states form square features in two-dimensional FWM, as indicated by the dotted rectangle in Fig. 3b.

To classify the features observable in two-dimensional FWM, we considered the response of a pair of two-level systems (TLS), coupled by different physical mechanisms[30]. We begin with two uncoupled TLS a and b of transition frequencies $\omega_{a,b}$ (Fig. 4a), each of them producing a single peak on the diagonal at (ω_a, ω_a) and (ω_b, ω_b) in the two-dimensional FWM signal. To discuss the coherent coupling mechanisms between the states, we first move to a single system representation (the resulting four-level system is shown in Fig. 4b). Without coupling, the states are product states $|0\rangle = |0\rangle_b|0\rangle_a$, $|1\rangle = |0\rangle_b|1\rangle_a$, $|2\rangle = |1\rangle_b|0\rangle_a$ and $|3\rangle = |1\rangle_b|1\rangle_a$, and their energies are the sum of the TLS state energies. Although there are transitions relating to off-diagonal peaks in this representation, they destructively interfere by construction, as shown in Fig. 4b. For example, the density grating in system a, described by the four-level density matrix elements ϱ_{11} and $\varrho_{00} = 1 - \varrho_{11}$, creates a third-order polarization in the off-diagonal elements ϱ_{31} and ϱ_{20} of opposite phase. In the schematic of the two-dimensional FWM signal, the off-diagonal signal at $(\omega_1, \omega_3) = (\omega_a, \omega_b)$ therefore cancels.

Depending on the coupling mechanism between a and b, this cancellation is lifted in different ways. For a biexcitonic coupling, which is given by an energy renormalization δ of the two-exciton state (for example, a static dipole–dipole or exchange interaction), the cancellation is lifted due to a spectral shift of the exciton–biexciton ϱ_{31} transition from ω_a to $\tilde{\omega}_a$, creating two separated off-diagonal peaks (Fig. 4c). Even if the renormalization is imaginary, that is, a dissipative coupling, the cancellation is lifted due to the different spectral widths of the two contributions.

If the interaction instead mixes the single exciton states, for example in a transition dipole (Förster, radiative) coupling[30,31], the two

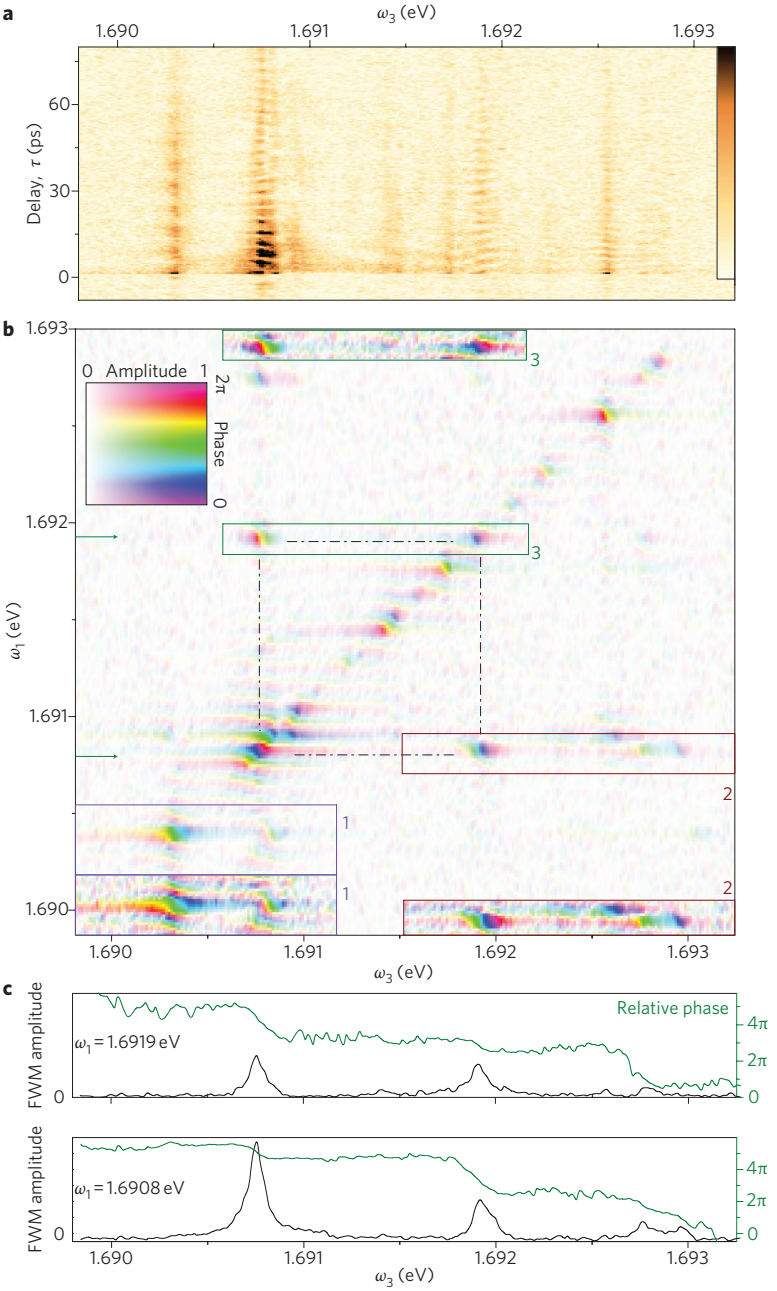

Figure 3 | Coherent coupling features observed in two-dimensional FWM in the region with high exciton density. Spectrally resolved FWM amplitude $|R_s^{-1,2}(\omega_3, \tau)|$ as a function of delay τ measured for the high-density region in Fig. 1d–f. Logarithmic scale over a factor of 11. **b**, Amplitude (saturation) and phase (hue) of the two-dimensional FWM $R_s^{-1,2}$ (ω_3, ω_1) resulting from **a** after Fourier transformation along τ. Linear scale from zero. The dashed-dotted square indicates coupled excitons at $\omega_3 = 1{,}690.75$ meV and $\omega_3 = 1{,}691.95$ meV. Insets 1–3 show regions, as indicated by the colour-coded frames on a four times smaller amplitude scale. **c**, Phase (green) and amplitude (black) profiles at $\omega_1 = 1{,}690.75$ meV and $\omega_1 = 1{,}691.9$ meV (see arrows in **b**) showing π-shifts over diagonal peaks and 2π-shifts over non-diagonal peaks. (For an intensity-only representation of **b** see Supplementary Fig. F.)

transitions remain at equal energy. However, the oscillator strength of the transitions is in general different, as the coupled exciton states are mixtures of the uncoupled ones, and the dipole moment is a phase-sensitive sum of the individual contributions. Their FWM amplitudes are therefore different, and the cancellation is lifted (Fig. 4d). The mixing also affects the decays of the transitions through the different radiative rates, leading to different linewidths, so that the off-diagonals show a more complex spectral shape (Supplementary Fig. H).

These two types of coherent coupling can therefore be distinguished by the shape of the off-diagonal signal. In the case of biexcitonic coupling, the biexcitonic peaks are spectrally shifted off the square edges $(\omega_{b,a}, \omega_{a,b})$, creating a doublet and a total phase shift of 2π over the off-diagonal. In the case of transition dipole coupling, the off-diagonal is a single peak at the square edges $(\tilde{\omega}_{b,a}, \tilde{\omega}_{a,b})$ with a π or 3π phase shift over the off-diagonal (Supplementary Fig. H). To support this qualitative discussion, we have numerically simulated the FWM signal of a four-level system with frequencies and transition dipole moments representing the different coupling mechanisms (for details, see Supplementary Appendix B), as shown in the bottom row of Fig. 4. A π shift can be observed over the diagonal terms and the non-diagonal elements resulting from the transition dipole coupling (Fig. 4d), whereas a 2π shift is seen over the off-diagonal elements for biexcitonic coupling (Fig. 4c), even if a double peak structure is not well resolved.

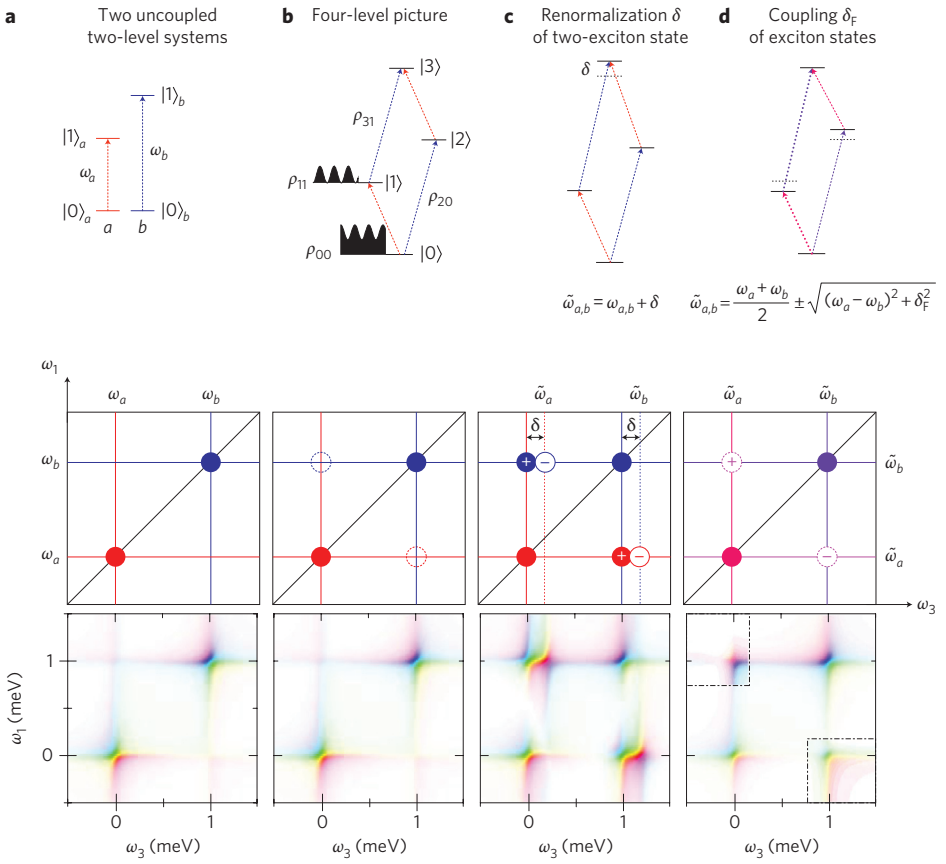

Figure 4 | Simulations of coupling features observable in two-dimensional FWM. a–d, Energy-level diagrams (top row) and corresponding sketches of two-dimensional FWM (middle row) for two uncoupled two-level systems $|0_{a,b}\rangle - |1_{a,b}\rangle$ exhibiting transition energies $\omega_{a,b}$ (**a**); a four-level system equivalent to **a** (**b**); a four-level system with biexcitonic coupling energy $\delta > 0$ (**c**); a four-level system with excitonic transition dipole coupling δ_F yielding modification of transition dipole strengths (**d**). Bottom row: amplitude- and phase-resolved simulations of two-dimensional FWM spectra for **a–d**. These were obtained from a time evolution of the density matrix under a sequence of two δ pulses[37] (Supplementary Appendix B). Parameters are equal uncoupled transition dipole moments and dephasing of $\gamma = 50$ μeV for all transitions. Energy splitting $\omega_a - \omega_b = 1$ meV. Energy scales are given relative to ω_a. **c** is as in **b**, but $\delta = 4\gamma$. **d** is as in **b**, but with ±10% modification of the transition dipole moments. Colour scale as in Fig. 2b. The non-diagonal regions in **d** (dashed–dotted squares) are shown, for clarity, with a three times smaller range of amplitude. (The simulated two-dimensional FWM intensity is shown in Supplementary Fig. I.)

To reveal the mechanism of coherent coupling observed in Fig. 3b, we therefore analysed the phase of the measured off-diagonal signal given in Fig. 3c. A π shift is observed for the diagonal peak, as expected for a single Lorentzian resonance. Conversely, the off-diagonal signals clearly demonstrate a 2π shift over the peak, showing that although not well separated in the amplitude spectra, off-diagonal elements consist of two resonances, each contributing a π shift to the phase. The underlying coupling is therefore of biexcitonic type, as depicted in Fig. 4c. Similar observations were made for measurements at many other sample positions where a significant off-diagonal signal was present. By analysing the off-diagonal signal in amplitude and phase (Supplementary Appendix A), we can determine the renormalization δ underlying the coherent coupling. For $\omega_3 \simeq 1{,}691.9$ meV in Fig. 3b, we find $\delta = (56 + 2i)$ μeV, with errors in the range of a few μeV. The real part represents an exciton–exciton repulsion, and the imaginary part, which reflects dissipative coupling and could be due to processes such as Auger recombination, is zero (within error). The same analysis for the second coupled state $\omega_3 \simeq 1{,}692.8$ meV results in $\delta = (187 - 3i)$ μeV. Similar values of δ were found for a number of other coherently coupled states, showing a repulsion of 10–200 μeV and negligible dissipative coupling.

Features characteristic of transition dipole coupling (Fig. 4d), where off-diagonal elements exhibit a π or 3π shift over the peak, have not been observed. This is in agreement with the radiative coupling energies of the order of 10 μeV at resonance and a distance of 100 nm, scaling with the inverse of the energy splitting and the inverse third power of the distance[31], resulting in an expected radiative coupling in the sub-μeV range. As an exception, fine-structure splitting is due to transition dipole coupling of the two spatially superimposed circularly polarized excitons, giving an estimate for the coupling strength at small distances. However, as fine-structure splitting comes with a strong biexcitonic coupling due to spatial overlap, the off-diagonal structure in this case is dominated by biexcitonic coupling features.

As the coupling of single excitons scales differently with their spatial separation for radiative and biexcitonic coupling, it is instructive to determine the distance between the coupled excitons. This is achieved by combining two-dimensional FWM spectroscopy with hyperspectral spatial imaging. Figure 5a–c shows the corresponding images at the energies of the coupled excitons of Fig. 3 (Supplementary Fig. J). One can see that the coherently coupled excitons observed at $\omega_3 = 1{,}690.75$ meV and 1,691.95 meV (blue arrow) are centred at the same position, suggesting that the coupling occurs within the same monolayer island. Conversely, the coherently coupled excitons at $\omega_3 = 1{,}690.35$ meV and 1,690.83 meV (red arrow) show a separation of $d = 0.8$ μm. Note that, from the spectral information, we can determine the centre of an excitonic transition with a precision better than the resolution, similar to the principle of the super-resolution microscopy technique STORM[32]. Coherent coupling between excitons spatially separated

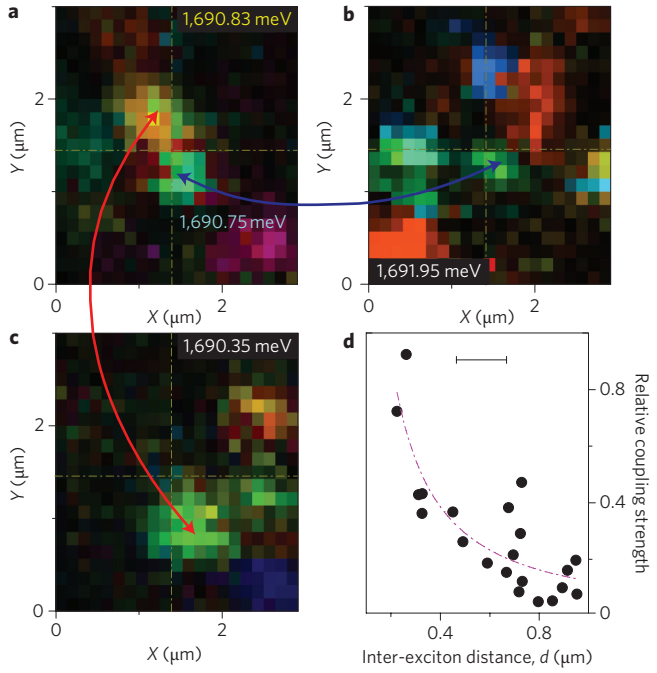

Figure 5 | Coupling strength as a function of inter-exciton distance. a–c, FWM intensity hyperspectral images around the position probed in Fig. 3, indicated with a cross. Colour scale as in Fig. 1. The coupled resonances visible in Fig. 3 are found to be spatially overlapping (**a**,**b**), or separated (**a**–**c**), as indicated by blue and red arrows, respectively. **d**, Relative coupling strength (RCS) as a function of distance between resonances, obtained on a high-density region of 20- to 21-monolayer quantum well thickness. A power law is fitted (purple dashed-dotted trace) giving RCS $\propto d^{-1.2\pm0.2}$. The error in d is estimated as 0.2 μm, and is indicated by the horizontal bar. The error in RCS falls within the symbol size.

by 0.1–0.9 μm has been identified in this way for many different cases. The coupling strength is evaluated by the ratio between the intensity of the off-diagonal signal and the geometrical average of the intensity of the diagonal signals. In this way, differences in oscillator strengths as well as spatial and spectral overlap of the excitation pulses are compensated. The measured coupling strength (Fig. 5d) shows a decay as a function of the inter-exciton distance. However, the decay is neither clearly exponential as expected for the spatial overlap of localized states nor dependent on d^{-3}, as expected for radiative coupling. We propose that the observed long-range coupling between excitons is enabled by extended excitons, as exemplified in Fig. 1e–f. Excitons of such large extension are not consistent with the expected localization of the exciton centre of mass motion, because the corresponding disorder potential is well below the expected residual disorder within a monolayer island by Al segregation of the order of 10–100 μeV. Specifically, using the localization length[33] $\xi_0 = \pi\hbar/\sqrt{2ME}$, we find for $\xi_0 =$ 1 μm a disorder potential energy of $E \approx 0.6$ μeV. As the radiative renormalization[27,34] in a disorder-free 5 nm GaAs/AlAs quantum well is of the order of 100 μeV, it can supercede the residual spatial disorder, so that the radiative coupling can result in motional narrowing, yielding a delocalization of the exciton over the monolayer island or terrace. We therefore propose that the observed large extension of exciton states is enabled by radiative coupling, and that these states can be seen as localized quantum well exciton polaritons, or excitons dressed by the photon field. The long-range coherent coupling is thus not directly due to radiative coupling but is instead an indirect result of it.

In conclusion, we have shown that by using methods of two-dimensional coherent nonlinear spectroscopy in the optical frequency range, it is possible to detect, quantify and physically interpret coherent coupling within discrete groups of excitons. The coupling mechanism is revealed through the spectral amplitude and phase of the off-diagonal signal of the coupled partners in two-dimensional FWM. For the monolayer localized excitons investigated in the present work, biexcitonic coupling is found to be the dominant mechanism, and no direct evidence of radiative coupling was found, even though coherent coupling between excitons spatially separated by up to 1 μm was observed. We propose that this long-range coupling is mediated by the observed extended exciton states, which form in extended monolayer terrace structures. The remaining short-range disorder due to segregation, which is expected to localize excitons to below 100 nm, seems to be overcome. We propose that this is due to exciton–polariton states formed by radiative coupling, which are averaging over the disorder. Radiative coupling is therefore important, not directly for the coupling of energetically separated states, but for the creation of extended states acting as coupling channels. The presented technique and the insight gained on coherent coupling can be applied to a variety of other nanostructures, and provides essential information on the mechanisms of coherent coupling of the contained individual quantum systems. Combining HSI with ultrafast pulse-shaping techniques for coherent control produces a characterization, control and readout technique suited for the implementation of quantum-information-processing algorithms.

Methods

Sample. In this Article, we examine individual localized excitons in a 5 nm GaAs/AlAs quantum well, grown by applying a growth interruption at both interfaces to allow the formation of large (~100 nm) monolayer islands at the interfaces[27,35]. Exciton states localized in these islands show a large oscillator strength due to their relatively large lateral size when compared to strongly confined excitons in InAs/GaAs self-assembled quantum dots. This makes them particularly well suited for measurement and manipulation by nonlinear optical techniques such as HSI. The sample was grown with a small thickness gradient over the wafer surface in the [110] direction, allowing the observation of a continuously varying spatial density of excitons localized in monolayer islands.

FWM experiment. The HSI technique was used to detect the FWM field[12] $R_s^{-1,2} \propto \mathcal{E}_2\mathcal{E}_2\mathcal{E}_1^*$ while varying the delay τ between excitation pulses 1 and 2 of fields $\mathcal{E}_1$ and $\mathcal{E}_2$ in a range of −20 to 100 ps, positive for pulse 1 leading. The typical total excitation fluence of the pulses was ~1 μJ cm^{-2}, created by a few thousand photons per pulse (Supplementary Table 1). Using a diffraction-limited spatial focus of 600 nm for excitation and confocal detection, HSI achieved a spatial resolution of 300 nm due to third-order nonlinearity, sufficient to measure the position and extension of the excitons[36]. At each spatial position, a spectrum of the response was acquired, creating a hyperspectral image of the excitons. This allowed the position and extension of the excitons to be measured to investigate their spatially non-local coupling.

Received 31 March 2010; accepted 10 November 2010; published online 19 December 2010

References

1. Lloyd, S. Quantum information matters. *Science* **319,** 1209–1211 (2008).
2. Borri, P. & Langbein, W. in *Semiconductor Quantum Bits* (eds, Henneberger, F. & Benson, O.) Ch. 12 (Pan Stanford Publishing, 2009).
3. Berezovsky, J., Mikkelsen, M. H., Stoltz, N. G., Coldren, L. A. & Awschalom, D. D. Picosecond coherent optical manipulation of a single electron spin in a quantum dot. *Science* **320,** 349–352 (2008).
4. Hanson, R., Dobrovitski, V. V., Feiguin, A. E., Gywat, O. & Awschalom, D. D. Coherent dynamics of a single spin interacting with an adjustable spin bath. *Science* **320,** 352–355 (2008).
5. Press, D., Ladd, T. D., Zhang, B. & Yamamoto, Y. Complete quantum control of a single quantum dot spin using ultrafast optical pulses. *Nature* **456,** 218–221 (2008).
6. Petta, J. R. *et al.* Coherent manipulation of coupled electron spins in semiconductor quantum dots. *Science* **309,** 2180–2184 (2005).
7. Koppens, F. H. L. *et al.* Driven coherent oscillations of a single electron spin in a quantum dot. *Nature* **442,** 766–771 (2006).
8. Foletti, S., Bluhm, H., Mahalu, D., Umansky, V. & Yacoby, A. *Nature Phys.* **5,** 903–908 (2009).

9. Li, X. *et al.* An all-optical quantum gate in a semiconductor quantum dot. *Science* **301,** 809–811 (2003).
10. Wu, T., Li, X., Duan, L. M., Steel, D. G. & Gammon, D. Density matrix tomography through sequential coherent optical rotations of an exciton qubit in a single quantum dot. *Phys. Rev. Lett.* **96,** 087402 (2006).
11. Nielsen, M. A. & Chuang, I. L. *Quantum Information and Quantum Computation* (Cambridge Univ. Press, 2000).
12. Langbein, W. & Patton, B. Heterodyne spectral interferometry for multidimensional nonlinear spectroscopy of individual quantum systems. *Opt. Lett.* **31,** 1151–1153 (2006).
13. Langbein, W. & Patton, B. Transient coherent nonlinear spectroscopy of single quantum dots. *J. Phys. Condens. Matter* **19,** 295203 (2007).
14. Hall, K. L., Lenz, G., Ippen, E. P. & Raybon, G. Heterodyne pump–probe technique for time-domain studies of optical nonlinearities in waveguides. *Opt. Lett.* **17,** 874–876 (1992).
15. Borri, P. *et al.* Measurement and calculation of the critical pulsewidth for gain saturation in semiconductor optical amplifiers. *Opt. Commun.* **164,** 51–55 (1999).
16. Lepetit, L., Chériaux, G. & Joffre, M. Linear techniques of phase measurement by femtosecond spectral interferometry for applications in spectroscopy. *J. Opt. Soc. Am. B* **12,** 2467–2474 (1995).
17. Langbein, W. & Patton, B. Microscopic measurement of photon echo formation in groups of individual excitonic transitions. *Phys. Rev. Lett.* **95,** 017403 (2005).
18. Kasprzak, J. *et al.* Up on the Jaynes–Cummings ladder of a quantum-dot/microcavity system. *Nature Mater.* **9,** 304–308 (2010).
19. Brixner, T. *et al.* Two-dimensional spectroscopy of electronic couplings in photosynthesis. *Nature* **434,** 625–628 (2005).
20. Zhang, T. *et al.* Polarization-dependent optical 2D Fourier transform spectroscopy of semiconductors. *Proc. Natl. Acad. Sci. USA* **104,** 14227–14232 (2007).
21. Stone, K. W. *et al.* Two-quantum 2D FT electronic spectroscopy of biexcitons in GaAs quantum wells. *Science* **324,** 1169–1173 (2009).
22. Bax, A. & Lerner, L. Two-dimensional nuclear magnetic resonance spectroscopy. *Science* **232,** 960967 (1986).
23. Wu, Q., Grober, R. D., Gammon, D. & Katzer, D. S. Imaging spectroscopy of two-dimensional excitons in a narrow GaAs–AlGaAs quantum well. *Phys. Rev. Lett.* **83,** 2652–2655 (1999).
24. Kasprzak, J. & Langbein, W. Vectorial four-wave mixing field dynamics from individual excitonic transitions. *Phys. Rev. B* **78,** 041103 (2008).
25. Erland, J. & Balslev, I. Theory of quantum beat and polarization interference in four-wave mixing. *Phys. Rev. A* **48,** 1765–1768 (1993).
26. Langbein, W. & Hvam, J. M. Localization-enhanced biexciton binding in semiconductors. *Phys. Rev. B* **59,** 15405–15408 (1999).
27. Savona, V. & Langbein, W. Realistic heterointerface model for excitonic states in growth-interrupted GaAs quantum wells. *Phys. Rev. B* **74,** 075311 (2006).
28. Gammon, D., Snow, E. S., Shanabrook, B. V., Katzer, D. S. & Park, D. Fine structure splitting in the optical spectra of single GaAs quantum dots. *Phys. Rev. Lett.* **76,** 3005–3008 (1996).
29. Patton, B., Woggon, U., Maingault, L., Mariette, H. & Langbein, W. Time- and spectrally-resolved four-wave mixing in single CdTe/ZnTe quantum dots. *Phys. Rev. B* **73,** 235354 (2006).
30. Danckwerts, J., Ahn, K. J., Förstner, J. & Knorr, A. Theory of ultrafast nonlinear optics of Coulomb-coupled semiconductor quantum dots: Rabi oscillations and pump–probe spectra. *Phys. Rev. B* **73,** 165318 (2006).
31. Parascandolo, G. & Savona, V. Long-range radiative interaction between semiconductor quantum dots. *Phys. Rev. B* **71,** 045335 (2005).
32. Hell, S. W. Far-field optical nanoscopy. *Science* **316,** 1153–1158 (2007).
33. Leosson, K., Jensen, J. R., Langbein, W. & Hvam, J. M. Exciton localization and interface roughness in growth-interrupted GaAs–AlAs quantum wells. *Phys. Rev. B* **61,** 10322–10329 (2000).
34. Andreani, L. C. & Pasquarello, A. Accurate theory of excitons in GaAs–$Ga_{1-x}Al_xAs$ quantum wells. *Phys. Rev. B* **42,** 8928–8938 (1990).
35. Gammon, D., Shanabrook, B. V. & Katzer, D. S. Excitons, phonons, and interfaces in GaAs/AlAs quantum-well structures. *Phys. Rev. Lett.* **67,** 1547–1550 (1991).
36. Kasprzak, J. & Langbein, W. Four-wave mixing from individual excitons: intensity dependence and imaging. *Phys. Status Solidi B* **246,** 820–823 (2009).
37. Axt, V. M., Kuhn, T., Vagov, A. & Peeters, F. M. Phonon-induced pure dephasing in exciton–biexciton quantum dot systems driven by ultrafast laser pulse sequences. *Phys. Rev. B* **62,** 125309 (2005).

Acknowledgements

The authors acknowledge support by the UK Engineering and Physical Sciences Research Council (EPSRC) (contract no. EP/D025303/1), and the European Commission under a Marie Curie Fellowship (FP7-PEOPLE-2007-2-1-IEF, 'CUSMEQ' contract no. 219762).

Author contributions

The experiments were designed by W.L., set up by W.L. and B.P., and performed by W.L. and J.K. Data were analysed by J.K. and W.L. Analysis tools were provided by W.L. and B.P. Theoretical modelling and interpretation were performed by W.L. and V.S.

Additional information

The authors declare no competing financial interests. Supplementary information accompanies this paper at www.nature.com/naturephotonics. Reprints and permission information is available online at http://npg.nature.com/reprintsandpermissions/. Correspondence and requests for materials should be addressed to J.K. and W.L.